Journal of Materials Chemistry A

ROYAL SOCIETY OF CHEMISTRY

PAPER

View Article Online
View Journal | View Issue

Cite this: J. Mater. Chem. A, 2023, 11, 1180

Structural engineering of metal–organic layers toward stable Li–CO_2 batteries†

Zhibin Cheng, ‡*ab Yanlong Fang,‡a Wen Dai,a Jindan Zhang, a Shengchang Xiang a and Zhangjing Zhang *ab

Received 3rd November 2022
Accepted 12th December 2022

DOI: 10.1039/d2ta08598d

rsc.li/materials-a

The rational design of metal–organic layers (MOL) with well-exposed catalytic sites and versatile structures holds great promise for boosting CO_2 reduction/evolution kinetics in Li–CO_2 batteries. In this work, a multifunctional MOL (Mn–TTA MOL) with a rich catalytic surface and flower-like conductive structure was fabricated as an efficient cathodic catalyst for Li–CO_2 batteries. Benefiting from the abundant accessible catalytic surface and unique conductive network, the as-developed cells based on the Mn–TTA MOL display high discharge capacity, low polarization, and excellent rate performance. Importantly, superior long-term cycling stability over 300 cycles can be achieved even at a high current density of 1.0 A g^{-1}. The findings provide new insights into catalyst engineering for high-performance Li–CO_2 batteries and would advance the development of MOL-based catalysts in various energy storage technologies.

Introduction

Carbon dioxide (CO_2) is regarded as a leading greenhouse gas and its excessive emission is accelerating atmospheric warming.[1] Targeting carbon neutrality, various sustainable technologies are explored to achieve cost effectiveness and environmental friendliness for CO_2 fixation. Li–CO_2 batteries have attracted intensive attention, which feature the possibility for synchronous implementation of carbon neutrality and development of advanced energy storage technologies.[2,3] Besides, as a new type of energy storage device, Li–CO_2 batteries provide a high theoretical energy density of 1876 W h kg^{-1} (based on the equation $4Li + 3CO_2 \rightleftharpoons 2Li_2CO_3 + C$) by converting the CO_2.[3,4] Compared to Li–O_2 batteries, Li–CO_2 batteries are more cost-effective and provide sustainable power for mechanical operation even in extremely CO_2-rich environments, which is a prospective energy source for future Mars exploration due to the fact that the air there contains 95% CO_2. Meanwhile, the Li–CO_2 battery is a platform to study the effect of CO_2 on Li–air batteries, providing valuable insight for the development of Li–air batteries under an air atmosphere.[3,5–7] However, sluggish CO_2 reduction and evolution reaction (CRR and CER) kinetics at cathodes inevitably deteriorate Li–CO_2 battery performance, which usually results in high overpotential, poor round-trip efficiency and low cycling stability.[5,8]

The key to addressing the above issues is developing highly efficient catalysts for the CRR and CER. Therefore, a variety of catalysts have been developed, including metal–organic frameworks (MOFs), porous carbon, metal-oxides/carbides and single-atom catalysts.[5,9–11] Among them, metal–organic frameworks (MOFs) have achieved remarkable achievements in catalyzing the conversion of CO_2 for high-performance cathodes.[12–17] However, the bulky nature of MOFs impedes the further enhancement of catalytic performance by reason of limited exposure of catalytic surface.[18–20] In this regard at least, lowering the size of bulky MOFs into two-dimensional (2D) metal–organic layers (MOLs) holds great promise for boosting CO_2 reduction/evolution kinetics due to their well exposed catalytically active sites and inherited structural advantages.[21–23]

MOLs can be prepared by a bottom-up approach, with selecting organic ligands and adjusting synthesis conditions.[24,25] The rational design of functional MOLs with excellent catalytic performance and a highly conductive network is indispensable for high-performance Li–CO_2 batteries. The ligand of perylene-3,4,9,10-tetracarboxylic dianhydride is usually inflexible with a large conjugate plane, and tends to form a 2D nanosheet in the synthetic process.[26,27] Moreover, conjugated carbonyl compounds have been regarded as promising cathodes in ion batteries due to their attractive structural tunability and redox reversibility.[28–30] Furthermore, suitable lone pair–π interactions have been considered to be an effective pathway for charge transfer in large conjugated systems.[31–33] The charge transfer of lone pair–π interactions efficiently strengthens the interactions among adjacent layers in MOLs

[a]Fujian Provincial Key Laboratory of Polymer Materials, College of Chemistry and Materials Science, Fujian Normal University, Fuzhou 350007, China. E-mail: chengzhibin@fjnu.edu.cn; zzhang@fjnu.edu.cn

[b]State Key Laboratory of Structural Chemistry, Fujian Institute of Research on the Structure of Matter, Chinese Academy of Sciences, Fuzhou, Fujian, 350002, China

† Electronic supplementary information (ESI) available: Experimental details, structural characterization, electrochemical measurements and tables. CCDC 2143640 and 2143641. For ESI and crystallographic data in CIF or other electronic format see DOI: https://doi.org/10.1039/d2ta08598d

‡ These two authors contributed equally to this work.

and hence forms highly conductive networks.[34–37] Thus, 1,6,7,12-tetrachloroperylene tetracarboxylic acid dianhydride (TTA) was considered as an ideal alternative ligand for the construction of MOLs with satisfactory catalytic performance and conductive networks.

To the best of our knowledge, rationally designed multifunctional MOLs have never been demonstrated for a rechargeable Li–CO_2 battery. Herein, as a proof of concept to demonstrate the feasible strategy based on MOLs for high-performance Li–CO_2 batteries, a multifunctional Mn–TTA MOL with a fully exposed catalytic surface and high electrical conductivity was prepared through the coordination reaction between $MnCl_2 \cdot 4H_2O$ and TTA. Besides, its crystal bulky counterpart (Mn–TTA MOF) was also fabricated to fully elaborate the structure advantage of the Mn–TTA MOL. And the as-fabricated flower-like Mn–TTA MOL was used as a cathodic catalyst for boosting the CRR/CER in Li–CO_2 batteries. Due to the synergy between the large catalytically active surface area and the stable conducting structure of the Mn–TTA MOL, the Li–CO_2 battery showed significantly enhanced performance in terms of specific capacity, rate capability and cycling stability. The Mn–TTA MOL cell offered remarkable performance improvement with a large discharge capacity of 22 229.4 mA h g^{-1}, a low overpotential of 1.11 V at 100 mA g^{-1}, and stable cycling up to 300 cycles at 1.0 A g^{-1} with a limited capacity of 1000 mA h g^{-1}.

Experimental

Material synthesis

Synthesis of Mn–TTA. $MnCl_2 \cdot 4H_2O$ (0.0197 g, 0.099 mmol) and 1,6,7,12-tetrachloroperylene tetracarboxylic acid dianhydride (TTA, 0.0028 g, 0.005 mmol) were dissolved in *N*,*N*′-dimethylacetamide (DMA)/H_2O (10 mL, v/v = 4 : 1) mixed solution at 80 °C for 2 days to afford brown transparent crystals of Mn–TTA. The crystals were collected and washed with DMA to remove the dyes on the surface of MOFs.

Synthesis of Zn–TTA. A mixture of $Zn(NO_3)_2 \cdot 6H_2O$ (0.012 g, 0.04 mmol) and TTA (0.0015 g, 0.002 mmol) was dissolved in the mixed solution of DMA/H_2O (8 mL, v/v = 7 : 1) and then heated in an oven at 80 °C for 2 days. After cooling to room temperature, light orange rod-shaped single crystals were obtained. The phase purity of the as-synthesized samples (Mn–TTA and Zn–TTA) was confirmed by powder X-ray diffraction (PXRD) technology.

Pre-processing of the CFP. Carbon paper was immersed in a mixture of nitric acid and hydrochloric acid (v/v = 1 : 3) at room temperature for 24 h, and then washed with deionized water, followed by drying at 85 °C for 24 h. After that, the acid-treated carbon paper was soaked in 0.1 M Mn^{2+} or Zn^{2+} aqueous solution for 24 h.

Preparation of the Mn–TTA MOL electrode. $MnCl_2 \cdot 4H_2O$ (0.099 g, 0.5 mmol) and TTA (0.023 g, 0.044 mmol) were dissolved in DMA/DMF/H_2O (5 mL, v/v/v = 4 : 0.5 : 0.5). After ultrasonic treatment for 10 min, the treated CFP was suspended on the surface of the solution at 100 °C for 9 h. Finally, the freshly prepared Mn–TTA/CFP was washed with anhydrous ethanol and dried at 65 °C for 12 h. For the bulky Mn–TTA MOF electrode, the synthesis was similar to that described for the Mn–TTA MOL electrode, except that the solvent was changed to DMA/H_2O (5 mL, v/v = 4 : 1).

Preparation of the Zn–TTA MOL electrode. $Zn(NO_3)_2 \cdot 6H_2O$ (0.120 g, 0.4 mmol) and TTA (0.023 g, 0.044 mmol) were dissolved in DMA/H_2O (6 mL, v/v = 5 : 1). After ultrasonic treatment for 10 min, the treated CFP was suspended on the surface of the solution at 100 °C for 9 h. Finally, the freshly prepared Zn–TTA MOL was washed with anhydrous ethanol and dried at 65 °C for 12 h.

Preparation of the Cr–Mn–TTA MOL electrode. $Cr(NO_3)_3 \cdot 9H_2O$ (0.100 g, 0.25 mmol) was dissolved in DMA/H_2O (20 mL, v/v = 18 : 2) mixed solvent. After ultrasonication for 10 min, the Mn–TTA MOL electrode was suspended on the surface of the solution for 6 h at room temperature. Finally, the freshly prepared Cr/Mn–TTA MOL was washed with anhydrous ethanol and dried at 45 °C for 12 h.

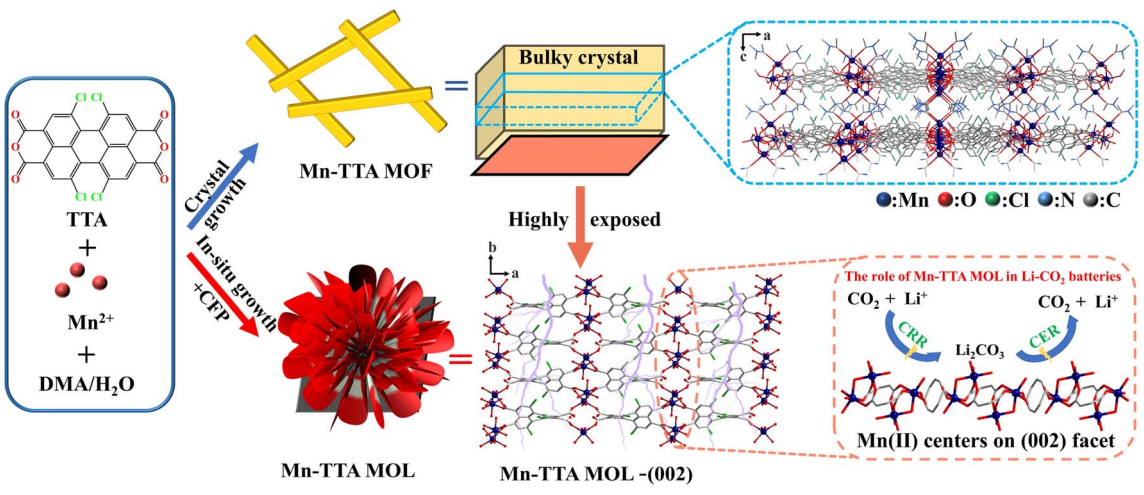

Fig. 1 Synthetic procedures for Mn–TTA MOF and Mn–TTA MOL.

Results and discussion

Bright yellow block crystals of Mn–TTA were prepared by a solvothermal reaction of TTA and $MnCl_2 \cdot 4H_2O$ in DMA/H_2O mixed solvent at 80 °C for 48 h. The single-crystal X-ray diffraction analysis showed that Mn–TTA belongs to the orthorhombic space group *Cmce*. Each independent six-coordination Mn center lies in a distorted double-pyramid geometry, and adjacent Mn atoms are further fused in a common vertex to form a $[Mn_2O(COO)_4(DMA)_2(H_2O)_2]$ binuclear cluster. Besides, each TTA ligand uses its four carboxylate groups in the mode of μ_2-κ^2O^1, O^2: κ^2O^{1a}, O^{2a} and μ-κ^1O^4: κ^1O^{4a} to link the six Mn(II) ions, as well as the DMA and H_2O molecules are linked to the Mn(II) ions in the mode of μ-κ^1O^6: κ^1O^{6a} and μ-κ^1O^8: κ^1O^7, respectively (Fig. S1, ESI†). The independent secondary building unit is laterally bridged by the TTA ligand and vertically terminated by DMA groups to afford an infinite 2D network (Fig. 1). The 2D layers are further stacked together along the *c* axis to form the bulky Mn–TTA MOF *via* the interlayer hydrogen bonding between the coordinated DMA molecules and H_2O molecules (Fig. 1). In addition, Zn–TTA with a 2D layered structure was also synthesized using the same procedures except changing the central metal (Fig. S2, ESI†). On the Mn–TTA (002) crystal facet, the coordinated solvent molecules at Mn(II) could be removed to form a coordination-unsaturated state (Fig. 1 and S1a, ESI†), which can act as the catalytically active sites in the discharge/charge process.[21,38] Therefore, Mn–TTA serving as a cathodic electrocatalyst for the Li–CO_2 cell holds great potential to promote the formation and decomposition of Li_2CO_3.

The torsion of the áromatic TTA ligand (torsion angle of 38.206°, Fig. S1b, ESI†) causes a lone pair–π interaction between two adjacent TTA molecules, and the shortest Cl···C distance is 3.308 Å (Cl1···C13) (Fig. 2a). Moreover, the shortest Cl···C distance in Mn–TTA is shorter than that of Zn–TTA, indicating strengthened lone pair–π interactions between two adjacent TTA molecules in Mn–TTA, hence resulting in a smooth charge transfer pathway to form a conductive network (Fig. S3, ESI†).[31,37,39–41] Besides, this result can also be visually demonstrated by X-ray photoelectron spectroscopy (XPS) analyses and infrared spectroscopy. The infrared absorption peak assigned to the C–Cl bond becomes wider for Mn–TTA. And the Cl 2p XPS spectrum in Mn–TTA shifts to a higher binding energy when compared to Zn–TTA and TTA (Fig. S3, ESI†).

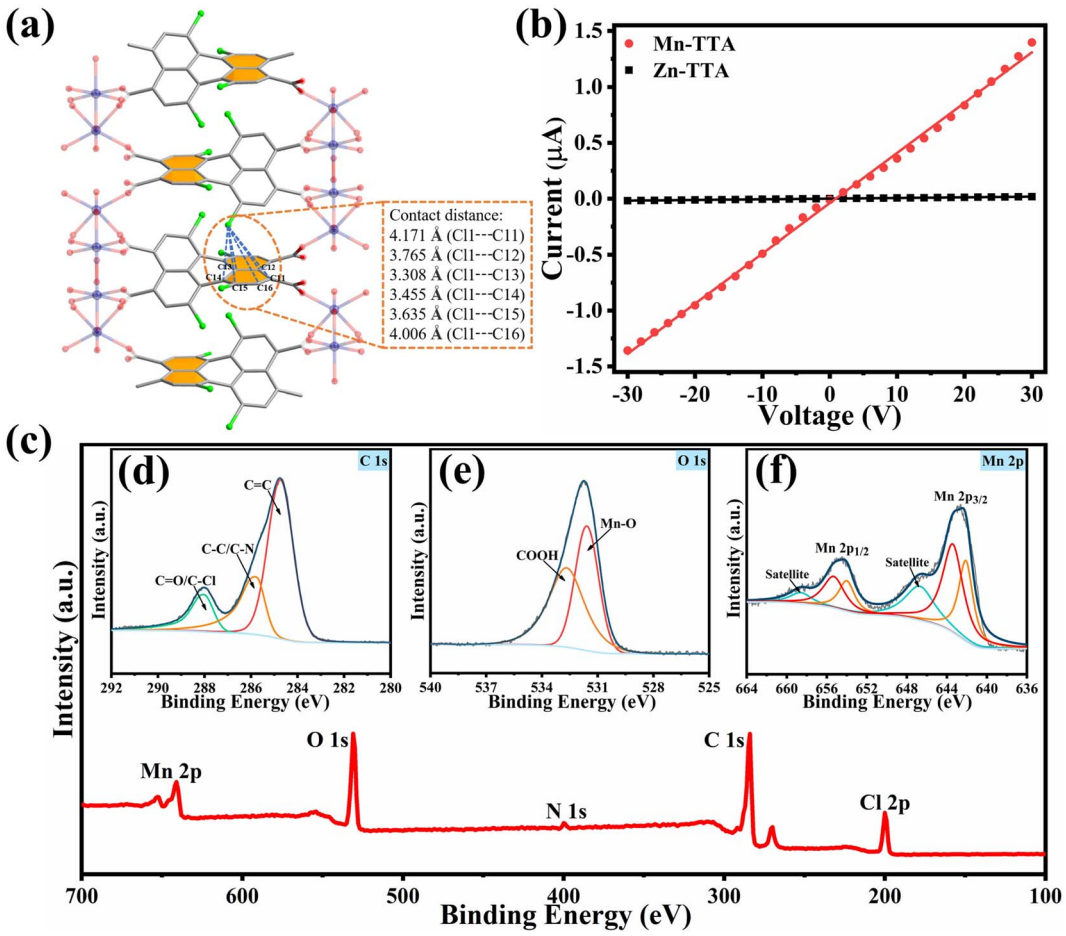

Fig. 2 (a) The TTA molecules connecting adjacent metal-oxide networks in Mn–TTA form a trapezoidal network (blue dotted line: intermolecular lone pair–π interaction); (b) the *I*–*V* curve of the pressed sample of Mn–TTA and Zn–TTA; (c) XPS survey spectrum, (d) C 1s XPS spectrum; (e) O 1s XPS spectrum and (f) Mn 2p XPS spectrum of Mn–TTA.

Remarkably, such a unique structure is highly beneficial for the rapid electron transfer of Mn–TTA MOL. In order to verify the effect of the intensified lone pair–π interactions on the conductivity, electrical conductivities of Mn–TTA and Zn–TTA were determined using a two-probe configuration. As presented in Fig. 2b, the Mn–TTA exhibits linear current–voltage characteristics, yielding a conductivity value of 1.43×10^{-7} S cm^{-1}, which is much higher than that of Zn–TTA (1.18×10^{-9} S cm^{-1}). The results provide an effective approach for engineering a high conductive network by reinforcing lone pair–π interaction in conjugated molecules. The surface chemical properties and chemical compositions of the electrocatalyst are crucial for catalytic conversion reactions. Thus, the surface chemical states of Mn–TTA are investigated by XPS. As illustrated in Fig. 2c, the XPS survey spectra of Mn–TTA exhibit five peaks at 642.8, 531.7, 400.1, 284.8 and 200.2 eV, corresponding to Mn 2p, O 1s, N 1s, C 1s and Cl 2p, respectively. The C 1s XPS spectrum can be deconvoluted into three subpeaks at 284.8, 285.5 and 288.2 eV (Fig. 2d), which are assigned to CC, C–C/C–N, and C–Cl/CO bonds, respectively. In addition, the existence of CO and C–Cl bonds could be verified using the infrared spectrum (Fig. S4, ESI†). The peaks at 531.5 eV and 532.8 eV in the O 1s XPS spectrum correspond to Mn–O and COOH carboxyl groups (Fig. 2e).[42,43] In addition, the high resolution spectrum of Mn 2p shows Mn $2p_{3/2}$ and Mn $2p_{1/2}$ peaks at 642.8 eV and 654.6 eV, and two satellite peaks located at 647.2 eV and 659.1 eV can be clearly distinguished.[44] Besides, the XPS results determined that these features are characteristic of Mn^{2+}, which is consistent with the valence calculations (Fig. 2f, Table S1, ESI†).[45] Based on the peak areas in the XPS spectrum, the estimated atomic ratio of Mn to O is 1 : 4.2, indicating the existence of unsaturated Mn atoms over the entire surface. The thermogravimetric analysis (TGA) further verifies the possibility of coordination solvent removal (Fig. S5, ESI†). More importantly, the vacancies left by escaping solvent molecules are favourable for chemisorption and catalytic sites for CO_2.[46–48]

To prepare the Mn–TTA MOL cathode for Li–CO_2 batteries (Fig. 3a), the Mn–TTA MOL was grown on carbon fiber paper (CFP) through the solvothermal reaction of TTA and $MnCl_2 \cdot 4H_2O$ in DMA/H_2O with an immersed CFP slip. Besides, the Zn–TTA MOL cathode was also prepared by a similar method except for changing the metal precursor. The morphology of the as-prepared catalysts was clearly revealed using a scanning electron microscope (SEM) and transmission electron microscope (TEM). The nanosheet morphology in the MOL is beneficial for the catalyst to expose more electrocatalytic active sites than that in the large size MOF (Figs. S6 and S7, ESI†). As shown in Fig. 3b and c, the 2D nanosheet-composed Mn–TTA MOL and Zn–TTA MOL flowers uniformly cover the surface of the CFP without additional binder. The uniform distribution of the flower-like Mn–TTA MOL catalyst in the composite cathode promises a highly accessible surface for adsorption and catalytic conversion of CO_2. In addition, the width of Mn–TTA nanosheets is about 1–3 μm, and the thickness can reach the nanometer level (Fig. S7, ESI†). The 2D plane of the Mn–TTA MOL corresponds to the Mn–TTA crystal plane (002), as validated by the XRD and crystal structure analysis (Fig. S8, ESI†). The (002) crystal facet of Mn–TTA is the crystallographically

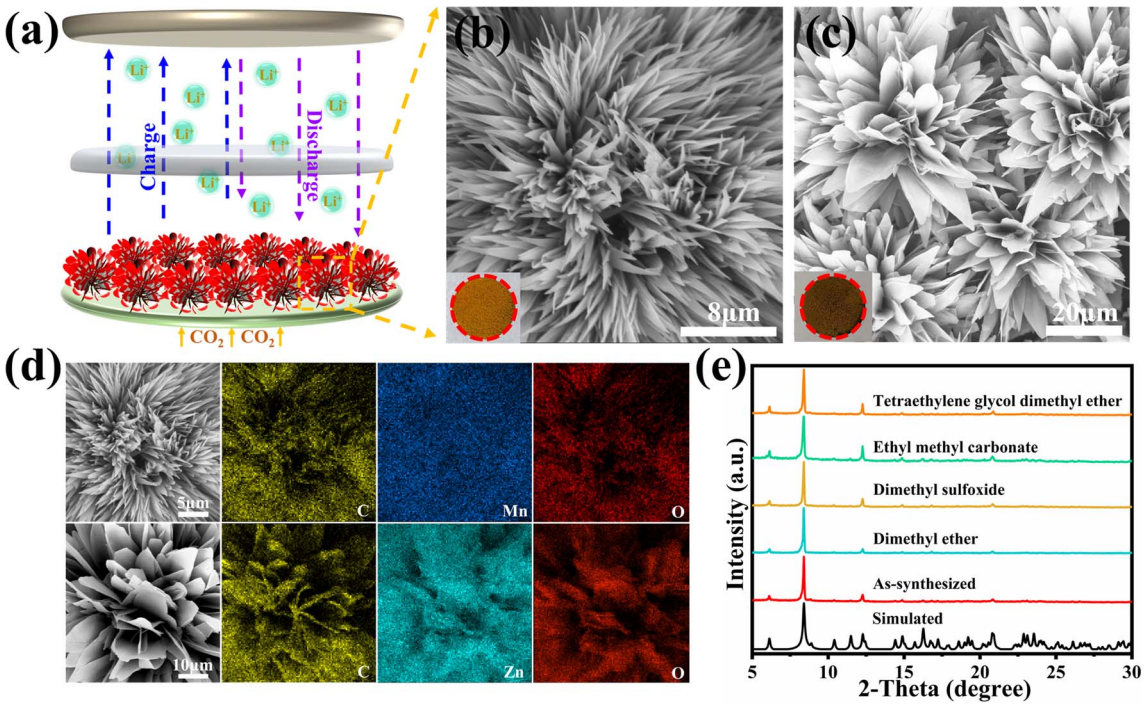

Fig. 3 (a) Schematic illustration of a Li–CO_2 battery: consists of a Li anode, nonaqueous electrolyte, separator and cathode. (b) SEM image of the Mn–TTA MOL. (c) SEM image of the Zn-TTA MOL. (d) SEM images and EDS core elemental mapping of the Mn–TTA MOL and Zn–TTA MOL. (e) Stability test results of Mn–TTA soaked in various solvents for 24 hours.

optimal growth direction, which exposes rich catalytic metal sites, thus providing high catalytic activity in the CRR and CER processes.[49,50] Meanwhile, Zn–TTA displays nanosheet-composed flower-like morphology analogous to Mn–TTA, which further reveals that the large rigid plane ligand tends to form a nanosheet structure (Fig. 3c and S9, ESI†). Furthermore, the elemental mapping images (EDS) of Mn, Zn, C and O combined with XRD analysis confirmed that the Mn–TTA MOL and Zn–TTA MOL were successfully grown on the CFP surface (Fig. 3d). Besides, Mn–TTA and Zn–TTA were soaked in various solvents for 24 hours to investigate their stability in electrolyte. As seen in Fig. 3e and S10 (ESI†), there is no obvious structure change after the soaking process, which indicates that both Mn–TTA and Zn–TTA have good corrosion resistance to the electrolyte. These characteristics make the Mn–TTA MOL very suitable for serving as a cathodic electrocatalyst for Li–CO_2 batteries.

To investigate the effects of the as-prepared cathodic catalysts on the electrochemical performance of Li–CO_2 batteries, coin cells with the lithium foil anode were fabricated. The cyclic voltammetry (CV) curves under CO_2 with a scan rate of 0.1 mV s^{-1} are shown in Fig. 4a, revealing that there are two peaks corresponding to the CO_2 evolution/reduction reaction in both Mn–TTA MOL and Zn–TTA MOL cells. To eliminate the possibility of background current from the reaction of the Mn–TTA MOL in this electrochemical window, the corresponding test was also performed under Ar (Fig. 4a). Obviously, no additional redox peaks could be detected, implying that the peaks observed under CO_2 ascribe to the CO_2 evolution/reduction reaction. Besides, negligible capacity is obtained under Ar, which is consistent with the CV result. In sharp contrast, a long discharge plateau is recorded in the presence of CO_2 (Fig. S11a, ESI†), demonstrating the high catalytic effect of the Mn–TTA MOL for CO_2 conversion. Additionally, compared with the Zn–TTA MOL cell, the Mn–TTA MOL cell displays higher current density and earlier onset potentials in the redox peaks, revealing that the electrochemical conversion of CO_2 is significantly improved on the Mn–TTA MOL surface. The promoted performance is probably due to the unique metal–organic layer structure and exposure of rich metal catalytic sites in the Mn–TTA nanosheet.

Furthermore, the galvanostatic full discharge tests were performed in the voltage range of 2.0–4.5 V at a current density of 100 mA g^{-1} (Fig. 4b). As expected, the discharge capacity of

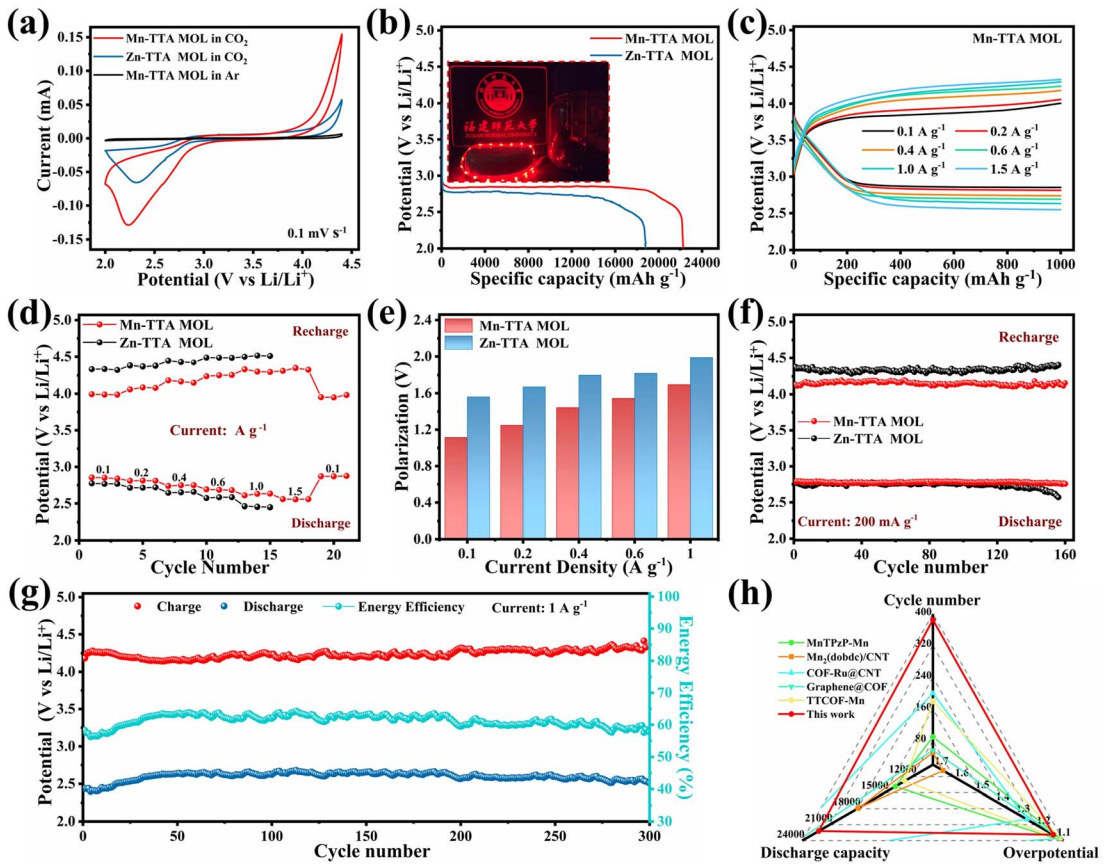

Fig. 4 (a) The cyclic voltammetry test at a scan rate of 0.1 mV s^{-1} within the potential window from 2.0 to 4.4 V. (b) Full discharge voltage curves at 100 mA g^{-1} (inset: eighteen red LEDs in parallel were lit brightly by the Mn–TTA MOL cell). (c and d) Rate performances within a limited capacity of 1000 mA h g^{-1} at various current densities. (e) Battery overpotentials at various current densities. (f) Cycling stability of Mn–TTA MOL and Zn–TTA MOL cells at a current density of 200 mA g^{-1}. (g) Cycling stability of the Mn–TTA MOL cell at a current density of 1 A g^{-1}. (h) Comparison of the electrochemical performance of the Mn–TTA MOL with other reported catalysts. The collected data are provided in Table S2, ESI.†

22 229.4 mA h g^{-1} for the Mn–TTA MOL cell was much higher than that for the Zn–TTA MOL cell (18 826.9 mA h g^{-1}), a further illustration of efficient catalytic performance of the Mn–TTA nanosheet (Fig. S11, ESI†). The rate performance was evaluated by increasing the discharge/charge current density from 0.1 to 1.5 A g^{-1}. The discharge end voltages for Mn–TTA MOL cells were 2.85, 2.73, 2.65, 2.63 and 2.54 V at current densities of 0.1, 0.4, 0.8, 1.0 and 1.5 A g^{-1}, respectively, significantly higher than those of Zn–TTA MOL cells (Fig. 4c and d). Importantly, the discharge end voltage could recover to the initial level when the current density was switched back to 100 mA g^{-1}, indicative of high reversibility for the Mn–TTA MOL cell. Besides, although the overpotential enhanced with the increase of current density, the Mn–TTA MOL cathode delivered a low overpotential of 1.68 V even at the high current density of 1.0 A g^{-1} (Fig. 4e and S12, ESI†), indicating an excellent rate performance due to the highly conductive flower-like Mn–TTA nanosheet with efficient catalytic activity for CO_2.

The cycling performances of the Mn–TTA MOL and Zn–TTA MOL cathodes at 200 mA g^{-1} with a limited capacity of 1000 mA h g^{-1} are provided in Fig. 4f. It can be clearly determined that the polarization voltage of the Zn–TTA MOL cathode starts to increase gradually after 150 cycles, while the Mn–TTA MOL cathode runs for 170 cycles with a smaller overpotential and shows no obvious decay of battery performance (Fig. S13a and b, ESI†). In addition, the cycle life of the Mn–TTA MOL cathode at a current density of 400 mA g^{-1} is much longer than that of the Zn–TTA MOL cathode, indicating its outstanding cycling stability (Fig. S13c, ESI†). The result can be attributed to the stable framework structure of Mn–TTA, which guarantees long-lasting catalytic activity (Fig. S14, ESI†). Furthermore, the cell can also afford stable cycling for 300 cycles with a decrease in overpotential from 1.75 V to 1.51 V even at a higher current density of 1000 mA g^{-1} (Fig. 4g), demonstrating the excellent catalytic performance of the Mn–TTA MOL. Benefiting from the design of the flower-like Mn–TTA MOL with rich exposed catalytic sites and a conductive structure, the resultant Li–CO_2 cell exhibits low overpotential, large discharge specific capacity, and stable cycling performance even at high current density. The electrochemical performance of the Mn–TTA MOL cell is comparable and even superior to that of recently reported metal–organic complex-based Li–CO_2 batteries (Fig. 4h and Table S2, ESI†).

To demonstrate the catalytic benefit of the central metal, chromium (Cr) was introduced into the coordination environment of Mn–TTA by the metal cation exchange method (Fig. S15, ESI†). Transition metals at the nodes for MOFs could be substituted with the preservation of the basic coordination scaffold.[51] After exchange, the characteristic peak associated with the (002) lattice

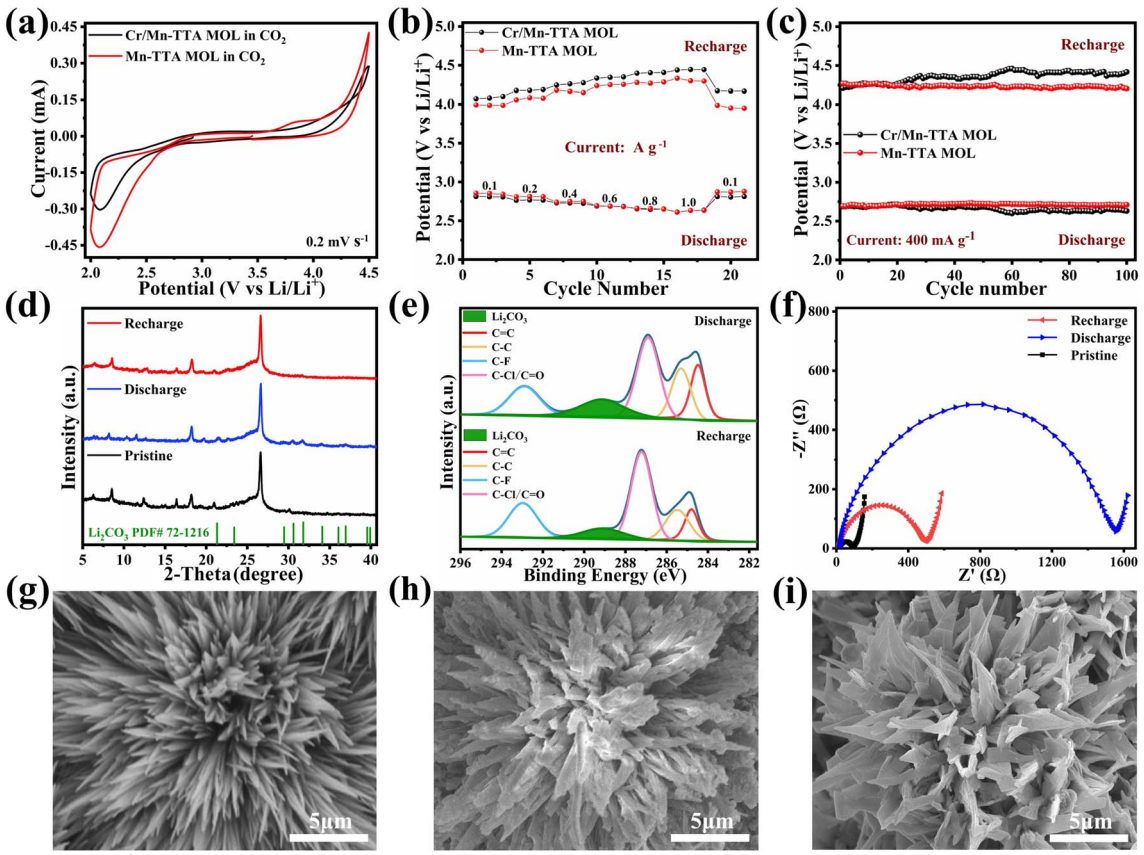

Fig. 5 (a) CV curves recorded at 0.2 mV s^{-1} within the potential window from 2 to 4.5 V under CO_2-saturated conditions. (b) Rate performances within a limited capacity of 1000 mA h g^{-1} at various current densities. (c) Cycling performance of Mn–TTA MOL and Cr/Mn–TTA MOL cells at a current density of 400 mA g^{-1}. (d) XRD patterns, (e) XPS spectra, (f) electrochemical impedance spectroscopy (EIS) spectra and (g–i) SEM image of the Mn–TTA MOL at pristine, discharge and recharge states.

plane for the Mn–TTA MOL is still retained while the peak intensity is weakened due to the size change (Fig. S16, ESI†). Additionally, the XPS spectra and the EDS results of the Cr/Mn–TTA MOL further verified the successful partial substitution of the central metal of the Mn–TTA MOL (Fig. S17, ESI†). Inductively coupled plasma optical emission spectroscopy (ICP-OES) analysis indicated a Cr : Mn molar ratio of 4.73 : 1. The subsequent electrochemical test for the Cr/Mn–TTA MOL was performed. The CV curves provided in Fig. 5a revealed more prominent two reaction peaks for the original Mn–TTA MOL cathode than for the Cr/Mn–TTA MOL cathode, demonstrating that the Mn–TTA MOL has a higher CRR/CER activity than the Cr/Mn–TTA MOL. As seen in Fig. 5b, the Cr/Mn–TTA MOL cell exhibited lower rate performance than the Mn–TTA MOL cell. Limited by the lower catalytic activity of the central metal, the Cr/Mn–TTA MOL cell could not maintain a low overpotential at large current density. The cycling performance was determined at a current density of 400 mA g^{-1} with a limited capacity of 1000 mA h g^{-1}. The observed relatively low cycling stability for the Cr/Mn–TTA MOL cell further confirms the low catalytic activity of the central metal Cr (Fig. 5c). The result demonstrates the feasibility of the application of the transition metal Mn in the catalytic system of cathodic electrocatalysts for Li–CO_2 batteries.

To verify the function of Mn–TTA in Li–CO_2 electrochemistry, discharged and recharged cathodes at different states disassembled from the Li–CO_2 batteries were carefully examined. As revealed in the XRD patterns (Fig. 5d), characteristic peaks for Li_2CO_3 were clearly observed after discharge, confirming the formation of the Li_2CO_3 discharge product.[5,52–54] After recharge, the XRD peaks associated with the Li_2CO_3 phase almost disappeared. Besides, XRD patterns of the Mn–TTA MOL have no detectable variation in the discharge/recharge process, implying good structure stability of the as-synthesized MOLs in Li–CO_2 batteries. Synchronously, compared with C 1s spectra for the discharged state, the peak located at 289.4 eV attributable to Li_2CO_3 is significantly weakened after recharge (Fig. 5e), indicating the reversible decomposition of Li_2CO_3.[55,56] Another new peak located at 293.0 eV originated from the electrolyte. Moreover, the characteristic peak in the Mn 2p XPS spectrum shifted to lower binding energy after recharge (Fig. S18, ESI†), which can be ascribed to the strong electron-donating ability of CO_2 and Li_2CO_3.[57,58] The intensity of the peak also decreases due to the formation of Li_2CO_3 on the Mn–TTA MOL surface. The recovery of the Mn 2p peak intensity after the recharge process further proves that the Mn–TTA MOL catalyst promotes the decomposition of Li_2CO_3.[59] In addition, compared with the pristine Mn–TTA electrode, the impedance of the cell increased significantly after discharge due to the precipitation of insulating Li_2CO_3 on the surface of the electrode in the discharge process. Subsequent recharging reduces the discharged state interfacial, charge transfer, and diffusion resistances, indicating that most of the insulating discharge product (Li_2CO_3) has been decomposed *via* the CO_2 evolution reaction in the charging process on the surface of the Mn–TTA MOL (Fig. 5f). To further elucidate the discharge and charge processes of the Mn–TTA MOL cell, the morphologies of discharged and charged cathodes were observed through SEM (Fig. 5g–i). In contrast to the morphology of the pristine state, the discharged Mn–TTA MOL cathode is covered with many discharge products from the surface (Fig. 5h). After recharge, most of these discharge products disappeared on the surface of the Mn–TTA MOL cathode, indicating the successful decomposition of Li_2CO_3. Although it is difficult to trace the formation of carbon and intermediates, these results fully reveal that the reduction and evolution of CO_2 in Li–CO_2 batteries catalyzed by the Mn–TTA MOL is a highly reversible process (Fig. S19, ESI†).

Conclusions

A multifunctional MOL has been successfully designed and fabricated as the advanced cathodic catalyst for high-performance Li–CO_2 batteries. The Mn–TTA MOL catalyst features a unique flower-like conductive structure with exposure of rich catalytic sites, which effectively promote the formation and decomposition of Li_2CO_3. The resultant Mn–TTA cathode enables efficient operation of Li–CO_2 batteries in terms of low overpotential, high discharge capacity, good rate capability and long cycling stability even under high current density. Meanwhile, the reinforcing lone pair–π interaction in conjugated molecules provides an effective approach for the design of advanced Li–CO_2 batteries. This work would advance the development of MOL-based catalysts in various energy storage technologies.

Conflicts of interest

There are no conflicts of interest to declare.

Acknowledgements

We acknowledge the financial support by the National Natural Science Foundation of China (22005054, 22101048, 21805039, 21971038, and 21975044), Natural Science Foundation of Fujian Province (2021J01149) and State Key Laboratory of Structural Chemistry (20200007).

Notes and references

1 Z. Zhang, Y. Zheng, L. Qian, D. Luo, H. Dou, G. Wen, A. Yu and Z. Chen, *Adv. Mater.*, 2022, **34**, 2201547.
2 Z. Xie, X. Zhang, Z. Zhang and Z. Zhou, *Adv. Mater.*, 2017, **29**, 1605891.
3 J. Xie, Z. Zhou and Y. Wang, *Adv. Funct. Mater.*, 2020, **30**, 1908285.
4 Y. Qiao, J. Yi, S. Wu, Y. Liu, S. Yang, P. He and H. Zhou, *Joule*, 2017, **1**, 359–370.
5 Q. Deng, Y. Yang, C. Mao, T. Wang, Z. Fang, W. Yan, K. Yin and Y. Zhang, *Adv. Energy Mater.*, 2022, **12**, 2103667.
6 J. H. Kang, J. Lee, J. W. Jung, J. Park, T. Jang, H. S. Kim, J. S. Nam, H. Lim, K. R. Yoon, W. H. Ryu, I. D. Kim and H. R. Byon, *ACS Nano*, 2020, **14**, 14549–14578.
7 Z. Cheng, Z. Wu, Y. Tang, X. Fan, J. Zhang, Y. Chen, S. Xiang and Z. Zhang, *Nanoscale*, 2022, **14**, 15073–15078.
8 B. Liu, Y. Sun, L. Liu, J. Chen, B. Yang, S. Xu and X. Yan, *Energy Environ. Sci.*, 2019, **12**, 887–922.

9 L. Z. Dong, Y. Zhang, Y. F. Lu, L. Zhang, X. Huang, J. H. Wang, J. Liu, S. L. Li and Y. Q. Lan, *Chem. Commun.*, 2021, **57**, 8937–8940.
10 F. Ye, L. Gong, Y. Long, S. Talapaneni, L. Zhang, Y. Xiao, D. Liu, C. Hu and L. Dai, *Adv. Energy Mater.*, 2021, **11**, 2101390.
11 Y. Zhang, R. Zhong, M. Lu, J. Wang, C. Jiang, G. Gao, L. Dong, Y. Chen, S. L. Li and Y. Lan, *ACS Cent. Sci.*, 2021, **7**, 175–182.
12 S. Li, Y. Liu, J. Zhou, S. Hong, Y. Dong, J. Wang, X. Gao, P. Qi, Y. Han and B. Wang, *Energy Environ. Sci.*, 2019, **12**, 1046–1054.
13 S. Li, Y. Dong, J. Zhou, Y. Liu, J. Wang, X. Gao, Y. Han, P. Qi and B. Wang, *Energy Environ. Sci.*, 2018, **11**, 1318–1325.
14 S. Xiang, Y. He, Z. Zhang, H. Wu, W. Zhou, R. Krishna and B. Chen, *Nat. Commun.*, 2012, **3**, 954.
15 R. Lin, S. Xiang, W. Zhou and B. Chen, *Chem*, 2020, **6**, 337–363.
16 Y. Chen, L. Zhang, H. Pan, J. Zhang, S. Xiang, Z. Cheng and Z. Zhang, *J. Mater. Chem. A*, 2021, **9**, 26929–26938.
17 H. Hong, J. He, Y. Wang, X. Guo, X. Zhao, X. Wang, C. Zhi, H. Li and C. Han, *J. Mater. Chem. A*, 2022, **10**, 18396–18407.
18 M. Lee, M. Shokouhimehr, S. Kim and H. Jang, *Adv. Energy Mater.*, 2021, **12**, 2003990.
19 A. Ahmad, S. Khan, S. Tariq, R. Luque and F. Verpoort, *Mater. Today*, 2022, **55**, 137–169.
20 J. Wang, S. Li, Y. Chen, L. Dong, M. Liu, J. Shi, S. Li and Y. Lan, *Adv. Funct. Mater.*, 2022, **32**, 2210259.
21 W. Yang, H. Wang, R. Liu, J. Wang, C. Zhang, C. Li, D. Zhong and T. Lu, *Angew. Chem., Int. Ed.*, 2021, **60**, 409–414.
22 Y. Shen, T. Pan, L. Wang, Z. Ren, W. Zhang and F. Huo, *Adv. Mater.*, 2021, **33**, 2007442.
23 Z. Chang, Y. Qiao, J. Wang, H. Deng and H. Zhou, *J. Mater. Chem. A*, 2021, **9**, 4870–4879.
24 L. Cao and C. Wang, *ACS Cent. Sci.*, 2020, **6**, 2149–2158.
25 X. Xiao, L. Zou, H. Pang and Q. Xu, *Chem. Soc. Rev.*, 2020, **49**, 301–331.
26 J. Zhao, M. Li, J. Sun, L. Liu, P. Su, Q. Yang and C. Li, *Chem. – Eur. J.*, 2012, **18**, 3163–3168.
27 B. Lu, Y. Chen, P. Li, B. Wang, K. Mullen and M. Yin, *Nat. Commun.*, 2019, **10**, 767.
28 X. Wang, C. Bommier, Z. Jian, Z. Li, R. S. Chandrabose, I. A. Rodriguez-Perez, P. A. Greaney and X. Ji, *Angew. Chem., Int. Ed.*, 2017, **56**, 2909–2913.
29 G. Zhou, Y. Miao, Z. Wei, L. Mo, F. Lai, Y. Wu, J. Ma and T. Liu, *Adv. Funct. Mater.*, 2018, **28**, 1804629.
30 M. Karlsmo, R. Bouchal and P. Johansson, *Angew. Chem., Int. Ed.*, 2021, **60**, 24709–24715.
31 J. Liao, J. Chang, L. Meng, H. Zhang, S. Wang and C. Lu, *Chem. Commun.*, 2017, **53**, 9701–9704.
32 X. Li, I. Angunawela, Y. Chang, J. Zhou, H. Huang, L. Zhong, A. Liebman-Pelaez, C. Zhu, L. Meng, Z. Xie, H. Ade, H. Yan and Y. Li, *Energy Environ. Sci.*, 2020, **13**, 5028–5038.
33 P. Li, J. M. Maier, E. C. Vik, C. J. Yehl, B. E. Dial, A. E. Rickher, M. D. Smith, P. J. Pellechia and K. D. Shimizu, *Angew. Chem., Int. Ed.*, 2017, **56**, 7209–7212.
34 M. Tang, S. Zhu, Z. Liu, C. Jiang, Y. Wu, H. Li, B. Wang, E. Wang, J. Ma and C. Wang, *Chem*, 2018, **4**, 2600–2614.
35 S. Fratini, M. Nikolka, A. Salleo, G. Schweicher and H. Sirringhaus, *Nat. Mater.*, 2020, **19**, 491–502.
36 Y. Xu, H. Sun, W. Li, Y. F. Lin, F. Balestra, G. Ghibaudo and Y. Y. Noh, *Adv. Mater.*, 2017, **29**, 1702729.
37 Y. Zou, T. Zhan, Y. Yang, Z. Fan, Y. Li, Y. Zhang, X. Ma, Q. Chen, S. Xiang and Z. Zhang, *J. Mater. Chem. A*, 2022, **10**, 3216–3225.
38 C. Yan, H. Li, Y. Ye, H. Wu, F. Cai, R. Si, J. Xiao, S. Miao, S. Xie, F. Yang, Y. Li, G. Wang and X. Bao, *Energy Environ. Sci.*, 2018, **11**, 1204–1210.
39 Z. Chang, Y. Qiao, J. Wang, H. Deng, P. He and H. Zhou, *Energy Storage Mater.*, 2019, **25**, 164–171.
40 D. A. Thomas, E. Mucha, M. Lettow, G. Meijer, M. Rossi and G. von Helden, *J. Am. Chem. Soc.*, 2019, **141**, 5815–5823.
41 C. F. Li, J. W. Zhao, L. J. Xie, J. Q. Wu, Q. Ren, Y. Wang and G. R. Li, *Angew. Chem., Int. Ed. Engl.*, 2021, **60**, 18129–18137.
42 Y. Zhang, J. Wang, S. Zhao, M. Serdechnova, C. Blawert, H. Wang, M. L. Zheludkevich and F. Chen, *ACS Appl. Mater. Interfaces*, 2021, **13**, 51685–51694.
43 Y. L. An, Y. Tian, Y. Li, C. L. Wei, Y. Tao, Y. P. Liu, B. J. Xi, S. L. Xiong, J. K. Feng and Y. T. Qian, *Chem. Eng. J.*, 2020, **400**, 125843.
44 Y. Li, L. Lin, R. Mu, Y. Liu, R. Zhang, C. Wang, Y. Ning, Q. Fu and X. Bao, *ACS Catal.*, 2021, **11**, 849–857.
45 Q. Song, Y. Yang, F. Yuan, S. Zhu, J. Wang, S. Xiang and Z. Zhang, *J. Mater. Chem. A*, 2022, **10**, 9363–9369.
46 Z. Cheng, Y. Chen, Y. Yang, L. Zhang, H. Pan, X. Fan, S. Xiang and Z. Zhang, *Adv. Energy Mater.*, 2021, **11**, 2003718.
47 Z. Cheng, H. Pan, J. Chen, X. Meng and R. Wang, *Adv. Energy Mater.*, 2019, **9**, 1901609.
48 Z. Chang, H. Yang, Y. Qiao, X. Zhu, P. He and H. Zhou, *Adv. Mater.*, 2022, **34**, 2201339.
49 Y. Li, Y. Xu, Y. Liu and H. Pang, *Small*, 2019, **15**, 1902463.
50 Y. Wang, X. Xiao, Q. Li and H. Pang, *Small*, 2018, **14**, 1802193.
51 Y. He, Z. Yin, Z. Wang, H. Wang, W. Xiong, B. Song, H. Qin, P. Xu and G. Zeng, *Adv. Colloid Interface Sci.*, 2022, **304**, 102668.
52 F. Lin, F. Lv, Q. Zhang, H. Luo, K. Wang, J. Zhou, W. Zhang, W. Zhang, D. Wang, L. Gu and S. Guo, *Adv. Mater.*, 2022, **34**, 2202084.
53 W. Ma, S. Lu, X. Lei, X. Liu and Y. Ding, *J. Mater. Chem. A*, 2018, **6**, 20829–20835.
54 J. Lin, J. Ding, H. Wang, X. Yang, X. Zheng, Z. Huang, W. Song, J. Ding, X. Han and W. Hu, *Adv. Mater.*, 2022, **34**, 2200559.
55 G. Wu, X. Li, Z. Zhang, P. Dong, M. Xu, H. Peng, X. Zeng, Y. Zhang and S. Liao, *J. Mater. Chem. A*, 2020, **8**, 3763–3770.
56 Z. Zhang, W. Bai, K. Wang and J. Chen, *Energy Environ. Sci.*, 2020, **13**, 4717–4737.
57 Z. Wang, Y. Zhou, C. Xia, W. Guo, B. You and B. Y. Xia, *Angew. Chem., Int. Ed.*, 2021, **60**, 19107–19112.
58 S. N. Sun, L. Z. Dong, J. R. Li, J. W. Shi, J. Liu, Y. R. Wang, Q. Huang and Y. Q. Lan, *Angew. Chem., Int. Ed.*, 2022, **61**, 2207282.
59 Z. Zhang, C. Yang, S. Wu, A. Wang, L. Zhao, D. Zhai, B. Ren, K. Cao and Z. Zhou, *Adv. Energy Mater.*, 2019, **9**, 1802805.